Journal of Alloys and Compounds 1039 (2025) 183276

Contents lists available at ScienceDirect

Journal of Alloys and Compounds

journal homepage: www.elsevier.com/locate/jalcom

Correlating microstructure, heat treatment, and corrosion modes of AM7075-Ti alloy prepared by selective laser melting (SLM)

Rafael Emil Klumpp [a,b,c,*], Sajjad Akbarzadeh [a,c], Thomas Kairet [d], Vedi Ölmez [e], Alexandre Mégret [b,c], Fabienne Delaunois [b,c], Marie-Georges Olivier [a,c]

[a] Materials Science Department, Faculty of Engineering, University of Mons, 20, Place du Parc, Mons 7000, Belgium
[b] Metallurgy Department, Faculty of Engineering, University of Mons, 20, Place du Parc, Mons 7000, Belgium
[c] UMONS Research Institute for Materials Science and Engineering, 20, Place du Parc, Mons 7000, Belgium
[d] Sirris, Liège Science Park, Rue du Bois Saint-Jean 12, Seraing Liége 4102, Belgium
[e] Belgian Ceramic Research Centre, Av. du Gouverneur E. Cornez 4, Mons 7000, Belgium

ARTICLE INFO

Keywords:
Additive manufacturing
Selective Laser Melting
Corrosion
AM7075-Ti alloy
SVET

ABSTRACT

Additive manufacturing (AM) enables the production of metallic components from a wide range of alloys, offering advantages such as reduced carbon emissions, efficient material usage, and the exploration of novel compositions. Among these, the AM of lightweight, high-strength aluminum alloys holds importance for aerospace applications, although corrosion remains a critical concern. In this study, newly additively manufactured 7075-Ti aluminum alloys, produced by the Selective Laser Melting (SLM) process using Ti-coated aluminum powder, were subjected to different heat treatments. The corrosion behavior was evaluated by immersion tests in EXCO solution, according to ASTM G34–18, and monitored by global electrochemical techniques, such as electrochemical impedance spectroscopy (EIS), and local electrochemical techniques, such as the scanning vibrating electrode technique (SVET). The microstructure was analyzed and characterized by Electron Backscatter Diffraction (EBSD). The results highlight the critical role of heat treatments in influencing the corrosion modes, resistance and mechanical properties of AM7075-Ti alloys.

1. Introduction

The advent of AM changed the way that metal is manufactured today. This method has been used to generate metal components from various metal alloys, and has recently shown exponential growth in popularity, both in terms of technology and applications [1–7]. Reduced carbon emissions, net-shape production, efficient material usage, small-scale flexibility (prototyping), and the opportunity to study alloy compositions previously unattainable with traditional procedures, are just a few advantages of this approach [1–7]. The transport and aerospace sectors are particularly interested in employing AM to produce aluminum alloys, special Al–Zn–Mg–Cu (AM7075) alloys that are lightweight, strong mechanically, and widely used in aircraft [1–3,5,8]. Standard high-strength 7075 aluminum alloy typically suffers from issues such as hot cracking, porosity, and composition loss during the SLM process, and its high cracking susceptibility results in low processability, leading to parts with mechanical properties which are inadequate for aerospace applications [9,10]. In this sense efforts have been made to achieve a crack-free AM7075 alloy, and numerous research projects have examined AM by optimizing process parameters. Laser power, scanning speed, hatch spacing, layer thickness, and preheating temperature are the primary topics of these parameters. Crack formation was found to be greatly impacted by scanning speed and laser power [11–14]. Another strategy is the functionalization of the feedstock aluminum alloy powder [15,16]. Among these strategies, the addition of titanium (Ti) acts as a grain refiner [9]. In this study, the 7075 feedstock powders were previously functionalized with 1.% Ti via plasma treatment, following the process described in the Sirris/Materia Nova patent [17] for metal-coated aluminum alloy particles. This innovative technique forms a Ti coating on the surface of the powder particles, which helps reduce hydrogen-induced blistering, an issue identified as a primary cause of increased porosity and defect propagation in additively manufactured parts [10].

Rapid heating and cooling rates are produced in the AM process, and the heat treatments applied after production in order to enhance mechanical properties result in a microstructure which is significantly

* Corresponding author at: Materials Science Department, Faculty of Engineering, University of Mons, 20, Place du Parc, Mons 7000, Belgium.
E-mail address: rafahemil@hotmail.com (R.E. Klumpp).

https://doi.org/10.1016/j.jallcom.2025.183276
Received 24 March 2025; Received in revised form 21 August 2025; Accepted 24 August 2025
Available online 25 August 2025
0925-8388/

different from those produced using conventional production methods [1,7,18]. Nevertheless, the metal's composition and microstructure have a major impact on the corrosion resistance behavior [1,7,18,19].

The main strengthening phase for AM7075 is the η′-phase (nominally $MgZn_2$) precipitates, but θ-phase (Al_2Cu), S-phase (Al_2MgCu), β-phase (Al_8Mg_5) and T-phase ($Al_2Mg_2Zn_3$) can also be found [20–22]. From the corrosion behavior point of view, the presence of anodic intermetallic particles, in this case η′-phase ($MgZn_2$) induces a localized corrosion due to trenching of the Al-matrix surrounding the particles [1,20,22–26]. For the aerospace and transportation sector, localized corrosion poses a serious risk that affects the aesthetics and, more importantly, structural integrity of parts. To date research on the corrosion of Al alloys generated by AM has mostly focused on the Al-Si alloy class [1]. As mentioned earlier, the current efforts on the AM7075 alloy have focused mostly on SLM process optimization as a way to mitigate the creation of cracks [1,3,7,18,27].

Zhang et al. [28], for the AM7075 alloy, highlighted the preferential corrosion through holes, which was attributed to the formation of the local cell due to the non-uniform distribution of η′-phase (nominally $MgZn_2$) on the AM alloy. Beura et al. [29] investigated the corrosion behavior of an AM7075 alloy processed with the addition of titanium and boron carbide (B_4C) particles in the feedstock. Their EIS results indicated a reduction in corrosion resistance, characterized by increased cathodic activity and decreased surface film resistance. This behavior was attributed to the partially dissolved Ti and B_4C phases, introduced via particle addition, which acted as local cathodic sites and promoted galvanic effects. Liu et al. [30] investigated the corrosion behavior of an AM7075 alloy fabricated via friction stir additive manufacturing. Their electrochemical measurements and microstructure observations highlighted that the primary factor influencing its corrosion resistance is the stability of the passive layer, which is significantly affected by the anodic dissolution of precipitates. The corrosion rate is largely dictated by the size and spatial distribution of these precipitates; fine and continuously distributed precipitates can create a continuous corrosion path, facilitating intergranular corrosion. They also noted that the retrogression and re-aging (RRA) heat treatment increases the size and spacing of grain boundary precipitates, thereby enhancing corrosion resistance [30]. Choi et al. [31] studied the corrosion behavior of additively manufactured 7075 aluminum alloy with silicon addition under different heat treatments. Anodic polarization tests revealed that the T6 heat treatment significantly improved corrosion resistance. This improvement was attributed to a more uniform redistribution of alloying elements within the matrix during solution treatment, along with the formation of fine, well-dispersed precipitates during aging, which help reduce pathways for localized corrosion [31]. Gharbi et al. [22] studied the microstructure, hardness, and electrochemical response for AM7075 with/without T6 heat treatment and identified passive-like behavior for AM AA7075 without heat treatment and better corrosion resistance than the conventional AA7075 alloy [22]. Prashanth et al. [32] investigated the corrosion resistance of SLM AM Al-12Si with varying heat treatments using weight loss in a strong media (1 M HNO_3). They found that the weight-loss curves of the cast specimens and the as-prepared SLM were remarkably similar, suggesting that the corrosion behaviors of these materials are comparable [32].

In this work, the microstructure, heat treatments (T6 and T6 with double ageing) and immersion tests are associated with the electrochemical response of global (EIS) and localized (SVET) techniques on AM7075.

2. Experimental design

Plates of additive manufactured AA7075-Ti (Al-0.08Si-0.08 Fe-1.59Cu-3.06Mg-0.17Cr-4.88Zn-0.9Ti(wt%)) were fabricated by the Sirris Research Center and used for the experiments. The samples were prepared using a SLM280 of Nikkon SLM solutions, equipped with a 400 W laser in an argon atmosphere with resulting oxygen content of < 50 ppm. For comparison, a regular AM 7075-T3 sample was used as standard. AM7075-Ti samples were heat-treated in T6 and T6 + Double aging (DA) (110°C for 5 h and 150°C for 14 h) in an argon gas atmosphere, and the non-heat-treated AM 7075 sample was identified as AM7075–0. The T6 heat treatment for the AA7075 alloy is used in most mechanical applications and in aviation, and the T6 state has the highest yield and ultimate strengths [33]. However, the T6 treatment decreases the alloys corrosion resistance [7,27,33]. The DA process, which consists in an aging treatment, which solves the line in a two-phase region, and re-aging the alloy for an extended period of time at a low temperature, was applied to a set of samples (T6 + DA) in order to get a combination of strength and corrosion resistance [7,27,33].

All the samples were sequentially polished to a 1 μm surface finishing using SiC papers and diamond pastes before microscopy observation and global electrochemical tests. For the macrographs, in order to reveal the grain boundaries, the sample was exposed for 15 s to Weck's reagent (1 g NaOH + 4 g $KMnO_4$ + 100 mL deionized water) for a metallography attack.

An immersion test was carried out during the 24-hour exposition in EXCO solution (4 mol L^{-1} NaCl + 0.5 mol L^{-1} KNO_3 + 0.1 mol L^{-1} HNO_3) for the exfoliation corrosion test performed according to ASTM G34-2018.

Macro and microstructural characterizations of the alloys were carried out by optical microscopy (OM) using a KH 8700 Hirox Digital Microscope, and scanning electron microscopy (SEM-FEG) using a Model SU8020 microscope, equipped with an energy-dispersive X-ray spectroscopy (EDX) detector.

The Electron Backscattered Diffraction technique (EBSD, HKL channel 5, Oxford instrument) was used to characterize the microstructure of the samples. Electron microscopy was carried with the TESCAN GAIA 3 equipment, using an Oxford instrument Nordlys Max3 EBSD detector. For the EBSD analysis, the specimens were embedded, mechanically polished up to 1 μm with diamond paste and finished with OPS solution (colloidal silica suspension). Given the difficulty of polishing aluminum alloys mechanically, some scratches remained present on the studied maps. Samples were mounted on the stub with silver paste to avoid image shift during acquisition. EBSD data were collected on the 70° tilted sample at 20 KV using Oxford instrument AZTEC software. EBSD data were collected using a 0.08 μm step size. Different crystal phases were included for the EBSD mapping, especially for samples from additive fabrication. Special attention must be paid to the indexation of these when the different crystal phases are close to each other. Raw data were post-processed in Oxford Instruments Channel 5 software by removing spikes and reducing zero solutions with cyclic iterations (up to 6 neighbors).

EIS tests were conducted in 0.05 M Na_2SO_4 solution using a Bio-Logic potentiostat SP-300. A three-electrode system, comprising the working electrode, Pt counter electrode, and an Ag/AgCl (saturated KCl) reference electrode, and the sample as the working electrode with an exposed surface of 1 cm^2. EIS measurements were obtained in a Faraday cage from 50 kHz to 10 mHz at 10 points per decade with perturbation of 10 mV rms. The parameter fitting was performed with Zview® software.

SVET was employed to investigate the effect of heat treatment on AM7075 alloys immersed in a 15 mM NaCl solution (380 Ω cm resistivity). Measurements were performed using Applicable Electronics equipment, with key operational parameters set as follows: a vibrating electrode distance of 150 μm from the sample surface, a vibration frequency of 65 Hz, and a vibration amplitude of 45 μm. A platinum/iridium SVET probe with a 20 μm diameter was used, platinized in a solution containing 1 % (wt./wt.) lead (II) acetate and 10 % (wt./wt.) platinum chloride to enhance tip capacitance. The system was calibrated according to the instruction manual of the instrument, using the same 15 mM NaCl solution. The exposed surface area of the embedded samples was approximately 1.5 mm^2, confined using 3 M™ Scotchrap™ 50 tape. Prior to isolation, the samples were mechanically polished with sandpapers ranging from 800 to 4000 grit to enhance electrochemical

activity. To ensure the accuracy and reproducibility of the measurements, two independent SVET scans were performed on each sample, utilizing a 31 × 31 grid point matrix.

Mechanical properties were characterized in terms of hardness. Hardness was measured under 5 kgf with an EMCO device and an average of 10 measurements was taken.

3. Results

3.1. Microstructural characterization

Fig. 1 displays the initial characterization of AM7075-Ti, using optical microscopy. The cross-section view (surface perpendicular to the building platform, XZ) is depicted in Fig. 1(a). The distinctive melt pools (localized molten regions created by a laser source), produced by the AM method, which have characteristics like a half-cylindrical shape, can be seen in this illustration. A greater magnification was applied in Fig. 1(b) to display the melt-pool borders, which consist of a boundary between the melted zone and the surrounding material.

Fig. 2 shows that the top surface (surface parallel to the construction platform, XY) exhibits a ladder-like feature due to the extensive laser traces. These results are consistent with the literature [1,28,34–36].

Fig. 3 shows the EBSD band maps which exhibit a refined microstructure as the average particle size is less than 1 μm of ferret diameter for all conditions (cross-section - Fig. 3(a), (b), and (c), and top-view - 3 (e), (f), and (g), not-heat treated, T6 and T6 + DA, respectively). These finer grains were due to the high cooling rate associated with the additive manufacturing process. For comparison, a Band map of conventionally produced (laminated) AA7075-T3, was displayed and this presented higher grain sizes, below 40 μm of ferret diameter on the cross-section view (3(d)) and 69 μm of ferret diameter on the top surface view (3(h)). In the same sense, Fig. 4 displays the inverse pole figure (IPF) maps for all samples (cross-sections, Fig. 4(a), (b) and (c), and top-views 4(e), (f) and (g)). The not-heat treated, T6 and T6 + DA samples are characterized by a randomly distributed grain orientation on the cross section and the top view. This suggests that the rapid cooling rate associated with the SLM process contributes to the random distribution of grains, primarily due to the thermal gradients that arise during solidification. These gradients create varying cooling conditions across the material, which hinder the establishment of a uniform grain orientation. As a result, the microstructure tends to be characterized by a lack of directional grain growth [1,3] .

The EBSD phase maps are presented in Fig. 5. For all three conditions (not-heat treated, T6 and T6 + DA, respectively), the cross-sections (Fig. 5(a), (b), and (c)) and top-views (5(e), (f), and (g)) show the distribution of $MgZn_2$ phases in the surface alloy. The $MgZn_2$ phase, indicated in blue, is concentrated in the grain boundaries. This location could be attributed to the segregation of solute elements during solidification and subsequent thermal treatment. As the aluminum alloy solidifies, the partitioning of magnesium and zinc occurs, leading to the formation of intermetallic compounds at the grain boundaries. This phenomenon is often enhanced by the thermal gradients present during the SLM processing and heat treatments, which promote the

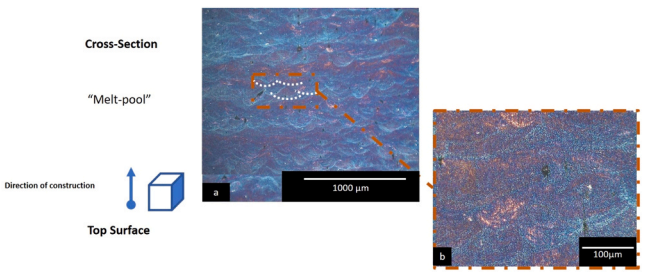

Fig. 1. Cross-section view of microstructure of AM7075-Ti Alloy.

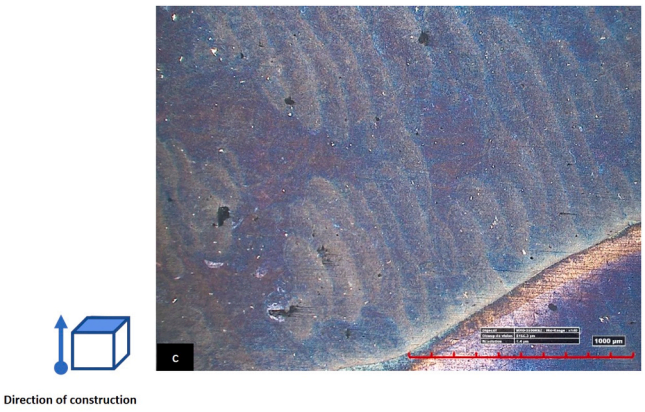

Fig. 2. Top surface view of AM7075-Ti Alloy.

accumulation of these solute-rich phases at the interfaces between grains [7,18].

Fig. 6 shows the SEM images for AM7075 with and without heat treatments. Fig. 6(a) and (d) show the surface aspect of the top surface and cross-section view of the not heat-treated sample respectively. It is possible to notice the presence of very fine intermetallic networks along the Al grain boundaries. This intermetallic network is presented in both views (Top surface and Cross Section). For a similar additive manufactured alloy (7075 not Ti functionalized), Gharbi et al. determined qualitatively, by transmission electron microscopy (TEM) analysis and EDS, that the fine network in the SLM7075 alloy is mainly composed of η-phase ($MgZn_2$), Mg–Cu–Zn(–Al) (ν-phase), Al–Cu–Fe–O, Mg_2Si, and precursor to η′-phase ($MgZn_2$) [22].

After the T6 heat treatment (Fig. 6(b) and (e) and T6 + DA, Fig. 6(c) and (f)), this intermetallic network is converted into coarse intermetallic particles spread over the surface. Fig. 7 presents the EDS maps of the samples highlighting the distribution of key elements (Cu, Mg, Ti, O, Al, and Zn). For the AM7075–0 surface, the EDS maps show that Cu, Mg, O, Al, and Zn are generally homogeneously distributed. However, Cu tends to concentrate in specific regions. Titanium (Ti), while not part of the intermetallic composition, exhibits a pattern of accumulation near the intermetallic network. On the AM7075-T6 surface, Mg, O, and Zn are evenly distributed. In contrast, Cu is localized within the intermetallic particles. Like AM7075–0, Ti accumulates near or within these particles. For the AM7075-T6 + DA surface, the maps display a homogeneous distribution of Mg, O, Al, and Zn. In this condition, Cu is also concentrated within the intermetallic particles, while Ti continues to show accumulation in their vicinity. The EDS composition analysis on the intermetallic particles, displayed in Fig. 8, confirms a significant presence of Cu (4.7 %), Mg (3.4 %), and Zn (9.5 %) within the AM7075–0 network structure. The EDS analysis of the intermetallic particles on the AM7075-T6 showed a significant presence of Cu (4.4 %), Mg (2.1 %), and Zn (5.1 %). The comparison between the AM7075–0 and the heat-treated AM7075-T6 samples reveals significant microstructural changes resulting from the T6 treatment. As observed earlier in the SEM images (Fig. 6), the AM7075–0 sample displays a finer, more dispersed intermetallic network, with elements such as Cu and Mg being more evenly distributed on the surface. In contrast, the T6-treated AM7075 sample shows the formation of distinct intermetallic particles, with Cu and Mg becoming concentrated within these particles, as indicated by the EDS analysis. The EDS composition analysis of the intermetallic particles on the AM7075-T6 + DA displays high concentrations of Cu (30.0 %) and Mg (8.1 %) suggesting that these elements are concentrated within the intermetallic particles formed during the T6 + DA process, contributing to the alloy's precipitation hardening. It is also observed that the titanium concentration experienced a further decrease following the T6 treatment. This reduction may be related to the dissolution of Zn at the 2-phase, coarsening the IM particles within the

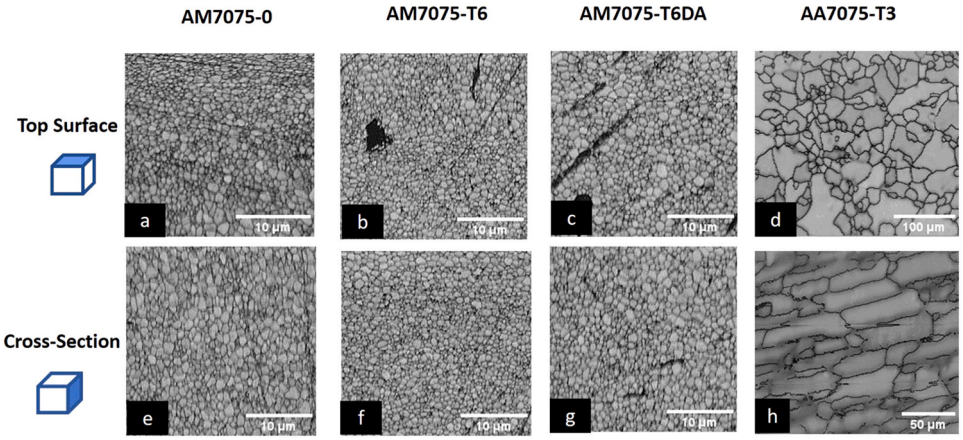

Fig. 3. EBSD Band maps - AM7075–0 top surface (a); AM7075-T6 top surface (b); AM7075-T6DA top surface (c); AA7075-T3 top surface (d); AM7075–0 Cross-section (e); AM7075-T6 Cross-section (f); AM7075-T6DA Cross-section (g), and AA7075-T3 Cross-section (h).

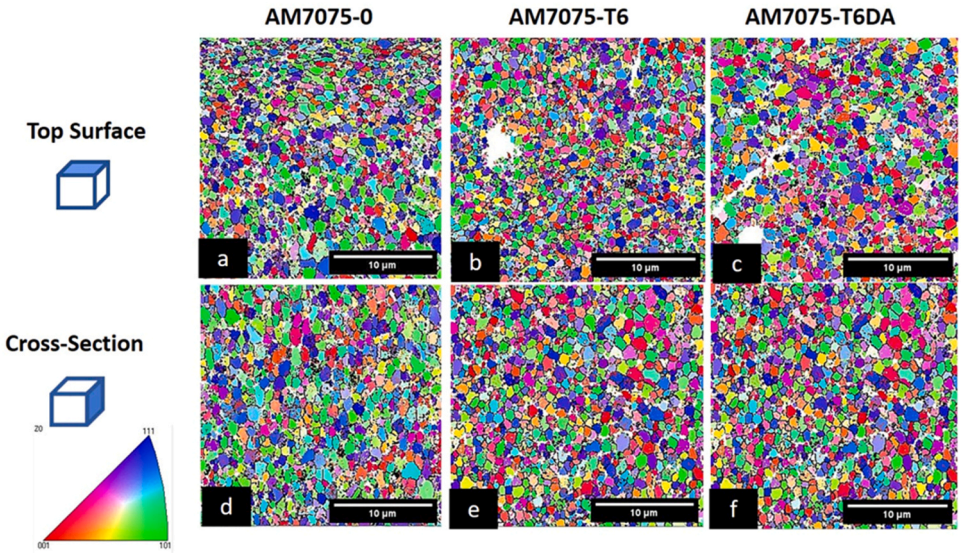

Fig. 4. Inverse pole figure maps (IPF_Z) - AM7075–0 top surface (a); AM7075-T6 top surface (b); AM7075-T6DA top surface (c); AM7075–0 Cross-section (d); AM7075-T6 Cross-section (e), and AM7075-T6DA Cross-section (e).

matrix during heating or its precipitation in nanometric forms (η'-phase η-phase) on the grain boundaries [33,37].

3.2. Electrochemical characterization

3.2.1. Electrochemical impedance spectroscopy (EIS)

Fig. 9 displays the EIS measurements (Nyquist and Bode plots) for the AM7075–0, heat-treated AM7075-T6, and AM7075-T6DA samples, measured in a 0.05 M Na_2SO_4 solution after 2, 4, and 6 h of immersion. The choice of 0.05 M Na_2SO_4 instead of 0.1 M NaCl was made to facilitate the visualization of the passive layer. Sulfate anions are less reactive than chloride ions and do not interfere with the electrode surface as much, helping to preserve the integrity of the passive layer and allowing for clearer and more accurate observation of its characteristics during electrochemical measurements. The AM7075–0 sample exhibited lower capacitive loops at Nyquist plots, Fig. 9(a), and lower |Z| values at low frequencies at Bode plot, Fig. 9(b), after 2, 4, and 6 h, suggesting lower resistance to charge transfer compared to the heat-treated samples. Although the Nyquist capacitive loops and |Z| values at low frequencies were very similar for the heat-treated samples, the AM7075-T6 sample showed greater modulus at low frequency compared to AM7075-T6DA, indicating slightly better corrosion resistance. In the Bode phase angle plot, *a* larger phase angle in absolute value (around −80°) was observed for the heat-treated samples (AM7075-T6 and AM7075-T6DA), indicating a more capacitive behavior. This suggests the presence of a stable and protective oxide layer. It is also noteworthy that the phase angle shifts to more negative values at lower frequencies, which further supports the presence of a more stable oxide layer. Such changes typically correlate with improved polarization resistance and a reduction in corrosion rates, reflecting the protective effect of the T6 heat treatment. Fig. 9(c) displays how the physical model is fitted for the samples after 2, 4 and 6 h of immersion, using two-time constants. The equivalent electrical circuit (EEC) model of two-time constants in parallel, which is used to describe electrochemical systems with both a passive layer and localized corrosion processes occurring concurrently [38]. For the EECs proposed, R_{sol} represents the electrolyte resistance. The CPE(oxide) (Constant phase element) and the resistor R(oxide) are related to a passive oxide layer formed on the surface, and the CPE_{dl} and R_{ct} are related to the corrosion processes surfaces, in special localized corrosion areas. This dual-time-constant model is particularly appropriate for aluminum alloys like AA7075, which form a passive layer but may also suffer from pitting corrosion in chloride-containing or aggressive environments. The parameter fitting was performed with Zview® software, which uses the nonlinear least-squares regression method to minimize

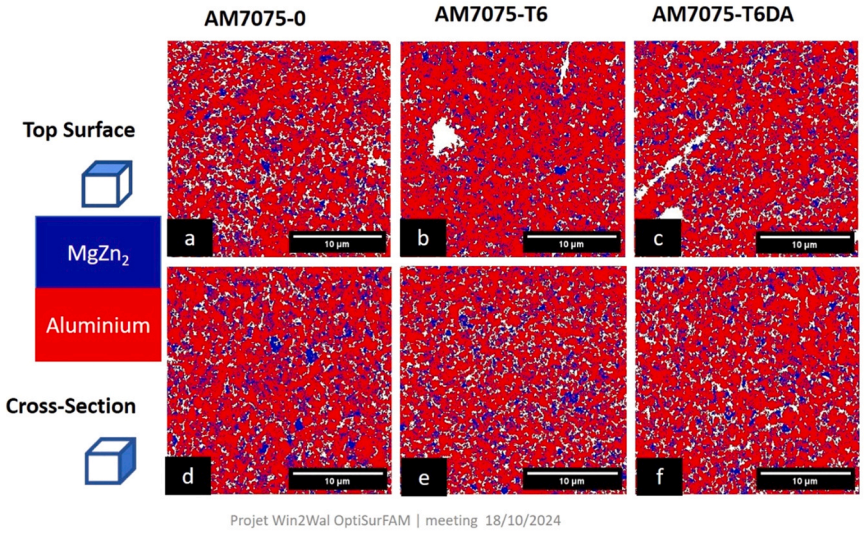

Fig. 5. EBSD phase maps - AM7075–0 top surface (a); AM7075-T6 top surface (b); AM7075-T6DA top surface (c); AM7075–0 Cross-section (d); AM7075-T6 Cross-section (e), and AM7075-T6DA Cross-section (e).

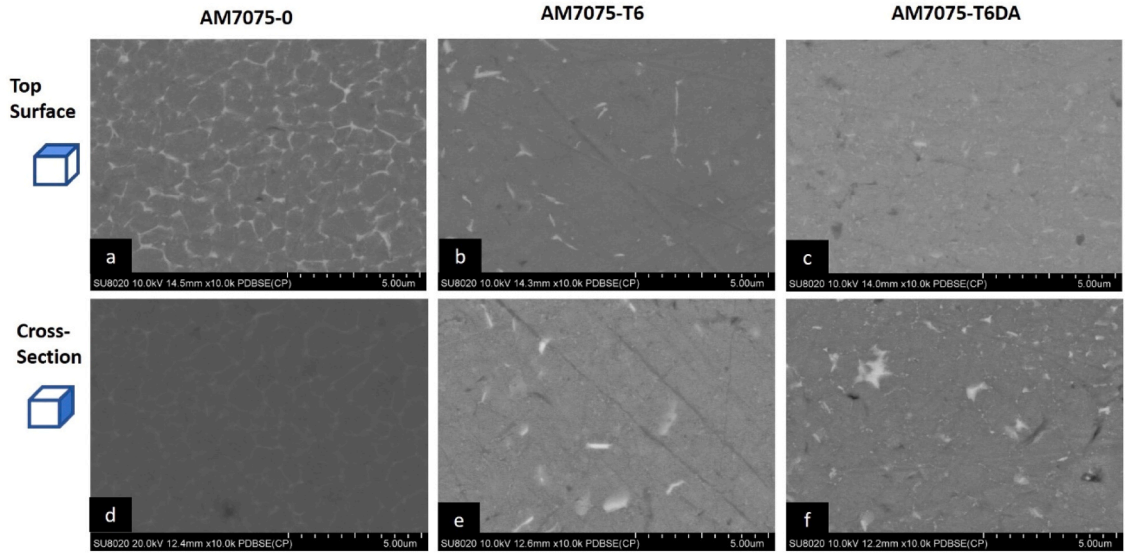

Fig. 6. SEM surface microscopy observation – AM7075–0 top surface (a), AM 7075-T6 top surface (b), AA7075-T6DA AA top surface (c), AM7075–0 cross section (d), AM7075-T6 cross section (e) and, AM7075-T6DA cross-section (f).

the difference between the experimental and simulated impedance spectra. The quality of the fit was assessed using the chi-square (χ^2) statistic and by visual comparison (supplementary material) of the fitted curves with the experimental Bode plots. The fitting results are presented in Table 1.

As observed in Table 1, the AM 7075–0 showed very high CPEdl values combined with an increasing Rct indicating a formation of a highly defective passive film. This behavior suggests poor passivation over a labyrinth-like network microstructure, Fig. 6(a), which is composed of nanometric η′-phase ($MgZn_2$) precipitates, η ($MgZn_2$), and a small fraction of dissolved Cu within the phases. This complex microstructure provides a highly electrochemically active area. The AM7075-T6 and AM7075-T6DA samples show initial values (6.35×10^{-6} $F.cm^{-2}.S^{(n-1)}$ and 6.62×10^{-6} $F.cm^{-2}.S^{(n-1)}$ respectively), indicating the initial capacitance behavior of their passive layers. The R(oxide), which represents the protection given by the oxide, showed significant differences between the alloys, particularly with the heat-treated samples (absent at the AM7075–0). The AM7075-T6 and AM7075-T6DA exhibited initial R_{ox} values, starting at 43,504 $\Omega.cm^2$ and 58,958 $\Omega.cm^2$ respectively. Over time, both alloys showed a significant increase in R_{ox}, with AM 7075-T6 reaching 64,364 $\Omega.cm^2$ and AM7075-T6DA reaching 70,360 $\Omega.cm^2$ at 6 h. This suggests that the T6 heat treatment and the additional aging process for AM7075-T6DA result in a more robust passive layer with better corrosion resistance in comparison. The capacitance value (CPE(dl)) is related to capacitance in the interface areas (metal-electrolyte in active corrosion areas). The results suggest, for all samples, that the overall electrochemical response of the surface becomes more stable over time. On the other hand, the R_{ct} values, which provide information about the resistance to electrochemical and charge transfer reactions at the electrode interface, also showed significant variation among the samples. AM7075–0 had lower R_{ct} values, starting at 42457 $\Omega.cm^2$ at 2 h and increasing to 75347 $\Omega.cm^2$ at 6 h, indicating moderate improvement in the charge transfer resistance, due the absorbed corrosion products acting as a barrier at the defects. AM7075-T6 and AM7075-T6DA exhibited higher initial R_{ct} values, with AM7075-T6 starting at 61,976 $\Omega.cm^2$ and reaching 123,000 $\Omega.cm^2$ at 6 h, and

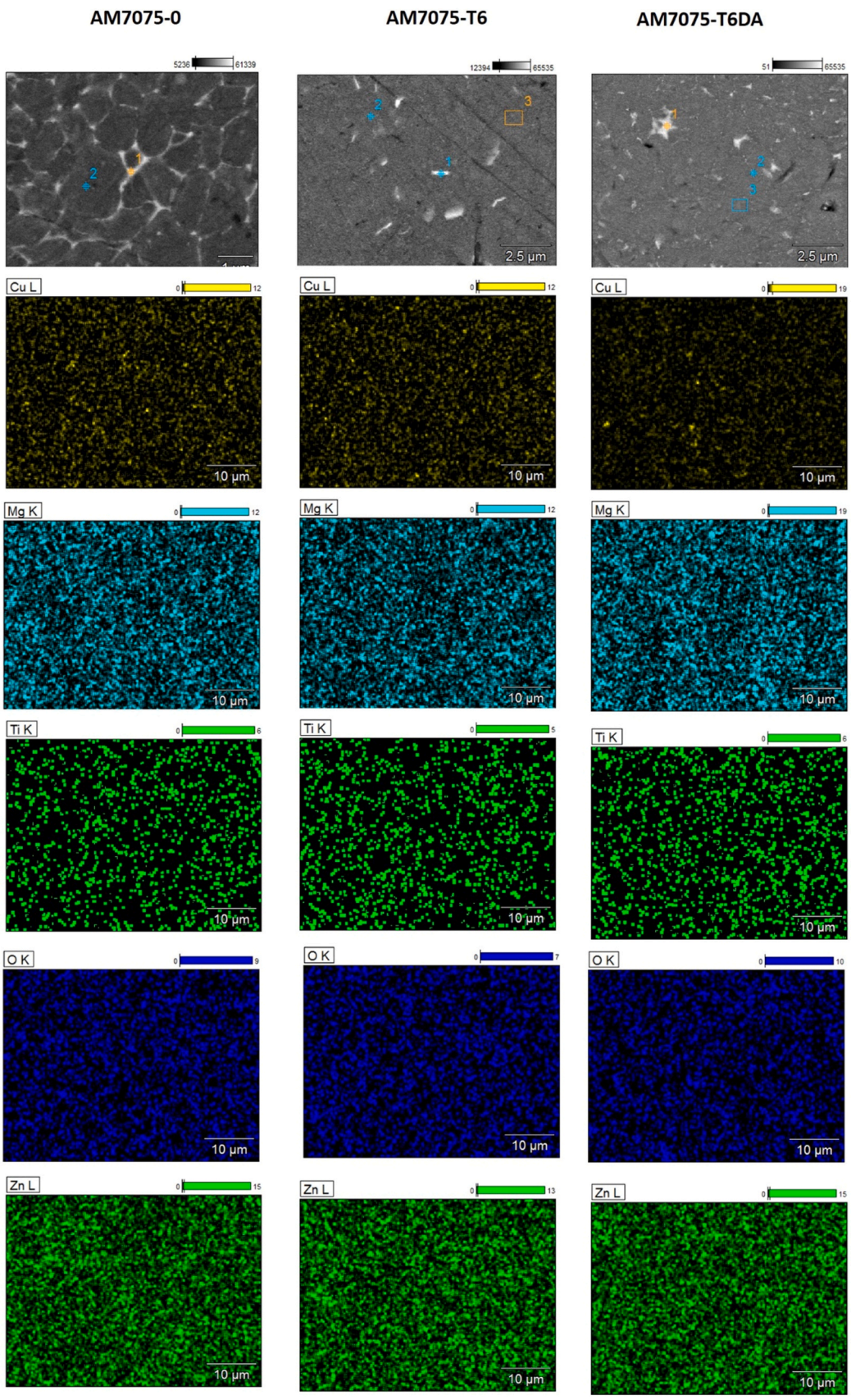

Fig. 7. SEM and Elemental EDS maps of AM7075–0, AM7075-T6 and AM7075-T6DA top surfaces.

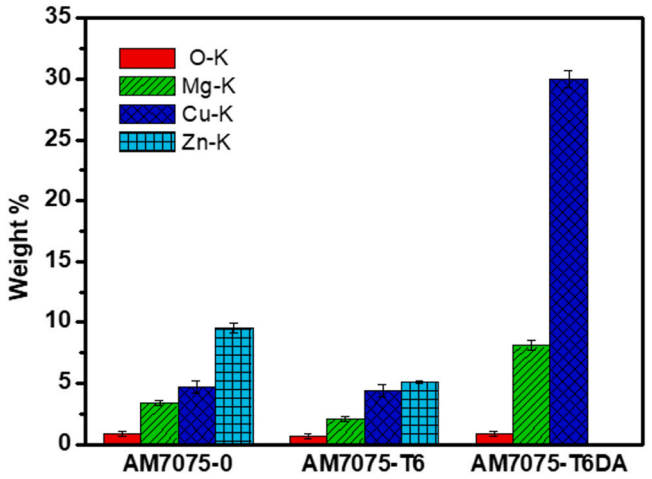

Fig. 8. EDS composition plots of intermetallic particles of AM7075–0, AM7075-T6 and AM7075-T6DA at top surface.

AM7075-T6DA starting at 83,547 Ω.cm^2 and reaching around 100,000 Ω.cm^2 by 6 h. The higher R_{ct} values in these samples suggest that both the T6 heat treatment processes result in a more resistant surface, with improved electrochemical stability and lower corrosion rates compared to the AM7075–0 alloy. The AM7075-T6 showed higher resistance to charge transfer and more stable electrochemical behavior, suggesting that the T6 treatment led to the formation of a more robust and protective passive layer.

The AM 7075-T6 condition exhibits a non-monotonic variation of CPEdl (12.0 → 12.4 → 11.0 × 10^{-6} F·cm^{-2}·S^{n-1}) alongside a steadily increasing Rct. This behavior probably arises because, at this stage, the alloy has not undergone complete aging and thus still contains metastable η′ ($MgZn_2$) precipitates at the surface, which is a nanometric needle-like precipitate dispersed on the surface [38–40], with segregations at the grain boundaries and defects. These Mg-rich particles promote localized galvanic interactions, reducing the homogeneity of the passive film. During the initial exposure (2–4 h), selective dissolution of η′ ($MgZn_2$) particles leads to a peak in electrochemical activity. Once these particles are consumed, repassivation occurs, and a more compact and stable oxide film is formed compared to AM 7075-T6DA. This increase is also observed in the np values (0.731 → 0.743 → 0.819), suggesting surface becoming more homogeneous.

In contrast, the AM 7075-T6DA condition, which results from double aging, promotes the transformation of metastable η′ into stable η ($MgZn_2$) precipitates (coarser) [38–40] [1–3]. The predominance of stable η precipitates and other coarse particles increases the galvanic activity between the aluminum matrix surface and intermetallic particles, as observed with higher CPEdl values (23.9 → 24.2 → 25.1 × 10^{-6} F·cm^{-2}·S^{n-1}) and lower np values (0.716→0.712→0.752) than AM 7075-T6. As a result, the oxide film formed under the T6DA condition is more susceptible to localized corrosion, as confirmed by SVET

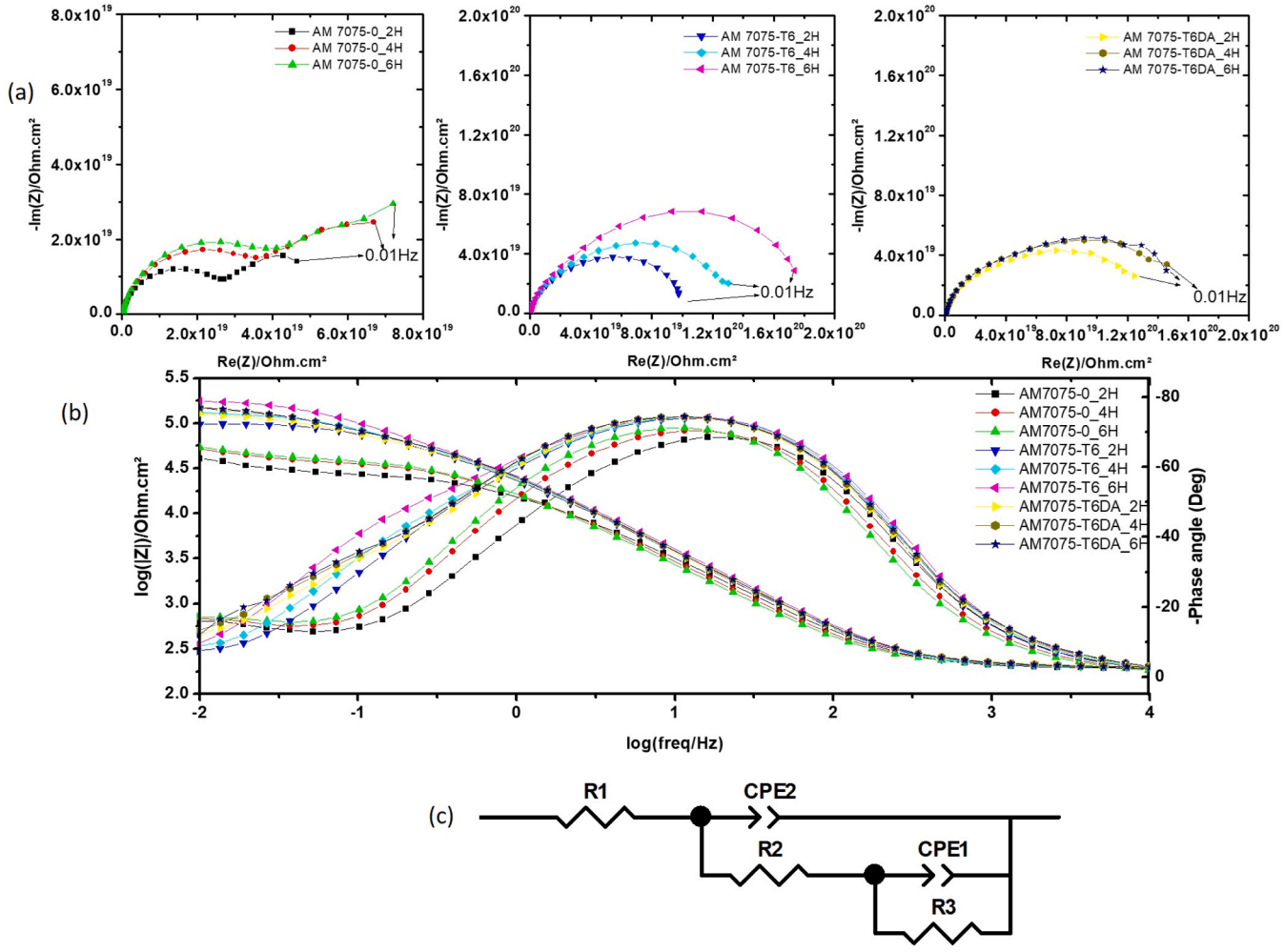

Fig. 9. Nyquist and Bode diagrams obtained by Electrochemical Impedance Spectroscopy in exposure to 0.05 mol L $^{-1}$ Na_2SO_4 solution after 2, 4 and, 6 h and EECs employed.

Table 1
Fitting results.

sample	exposure time (h)	CPE(oxide) ($F.cm^{-2}.S^{(n-1)}$)	n_p	R(oxide)($\Omega.cm^2$)	CPE_{dl} ($F.cm^{-2}.S^{(n-1)}$)	n_p	R_{ct} ($\Omega.cm^2$)	(χ^2) Chi-squared
AM7075–0	2	8.11×10^{-6}	0.899	25229	0.000199	0.759	42457	0.0004
AM7075–0	4	8.96×10^{-6}	0.898	34574	0.000137	0.755	65463	0.0003
AM7075–0	6	9.59×10^{-6}	0.897	37891	0.000130	0.744	75347	0.0002
AM7075-T6	2	6.35×10^{-6}	0.905	43504	12.00×10^{-6}	0.731	61976	0.0002
AM7075-T6	4	6.20×10^{-6}	0.902	51384	12.4×10^{-6}	0.743	86155	0.0001
AM7075-T6	6	6.01×10^{-6}	0.896	64364	11.0×10^{-6}	0.819	123200	0.0001
AM7075-T6DA	2	6.62×10^{-6}	0.896	58958	23.9×10^{-6}	0.716	83547	0.0003
AM7075-T6DA	4	6.57×10^{-6}	0.892	69670	24.2×10^{-6}	0.712	100330	0.0003
AMz7075-T6DA	6	6.53×10^{-6}	0.892	70360	25.1×10^{-6}	0.752	99414	0.0003

measurements, Fig. 10.

3.2.2. Local electrochemical examination (SVET)

The SVET analysis (Fig. 10), combined with optical and FESEM observations (Fig. 11), was performed on the mounted sample after 16 h of immersion in a 15 mM NaCl electrolyte, where the exposed area was restricted to 1.5 mm^2. In the AM7075–0 sample, localized anodic activity (red spots) was initiated early during immersion and intensified over time. Consistent with previous discussions, the susceptibility of the alloy to localized corrosion is considered a significant drawback. The images captured at the end of the test clearly illustrate bright regions corresponding to anodic activity and dark regions associated with cathodic activity. Both the SVET maps and imaging confirm the localized corrosion of AM7075–0, mainly at a specific spot within the exposed area, which progressively intensified over the immersion period. For the AM7075-T6 alloy, localized corrosion was initiated early during immersion, as depicted by the reddish-orange zones. However, the anodic activity decreased progressively over time, eventually transitioning to an inactive or cathodic site. This observation, which correlates well with the EIS data, highlights the ability of the alloy to repassivate and mitigate localized corrosion. The formation of corrosion products with effective barrier properties contributed to this behavior, leading to the development of a homogeneous layer, as observed in the imaging after the test. The localized electrochemical response of the AM7075-T6DA sample lies between that of the other two samples. From the beginning to the end of exposure, progressive anodic activity was observed, although its intensity remained lower compared to the AM7075–0 sample. Optical and FESEM images at the end of the test, in strong correlation with the SVET map, revealed the presence of corrosion products in the cathodic regions, appearing as black spots. The applied heat treatment caused a redistribution of elements, particularly Cu, shifting from homogeneous enrichment at the grain boundaries to being concentrated predominantly in coarse IMPs. This redistribution altered the corrosion behavior, transitioning from both intergranular and transgranular corrosion observed in AM7075–0 to predominantly intergranular corrosion in the heat-treated samples. The intensification of the corrosion phenomenon from AM7075-T6 to AM7075-T6DA is likely attributed to the increased concentration of Cu in the IMPs resulting from the double-aging process.

3.2.3. FESEM/EDS observation after SVET

After immersion in 15 mM NaCl, the SVET samples underwent FESEM/EDS analysis to investigate the corrosion products in terms of both chemical composition and morphology (Fig. 11). Three distinct topographical features of the corrosion products were identified across the alloys, revealing the critical role of the heat treatment process in determining corrosion resistance. For the AM7075–0 sample, relatively intense localized corrosion manifested as a pit surrounded by cracks. The EDS mapping revealed a depletion of Al and Mg near the cracks and pit, while Si and Mg were enriched in the corrosion products, indicating the formation of silica-based and partly magnesium-based compounds. For the AM7075-T6 sample, a uniform protective film was formed, with no signs of significant corrosion deterioration. This observation aligns well with the EIS and SVET results, which highlighted the development of a barrier layer during immersion. EDS analysis revealed a homogeneous distribution of Al, O, Zn, Mg, Si, Cu, and Ti across the surface. Notably, the depletion of aluminum, the primary component of the alloy, was considerably less pronounced compared to the AM7075–0 sample, further emphasizing the superior corrosion resistance imparted by the heat treatment. For the AM7075-T6DA sample, degradation had taken place in the form of severe localized corrosion, which was larger in size compared to the AM7075–0 sample. As previously discussed, heat treatment led to the accumulation of elements within the coarse IMPs, transferring the fine network of IMPs typically observed at the grain boundaries to accumulation in coarse IMPs. During immersion, these coarse IMPs were subjected to corrosion, dissolving and leaving pits in the alloy. The localized accumulation of IMPs resulted in higher elemental concentrations, contributing to the formation of larger pits than those observed in AM7075–0, but without the presence of cracks. The dissolution and subsequent detachment of these coarse IMPs from the alloy's surface likely explains the observed corrosion mechanism in AM7075-T6DA. However, the presence of cracks, particularly for AM7075–0, indicates the selective dissolution of the nanometric η'-phase at the grain boundaries. The cracks in AM7075–0 are attributed to the presence of fine intermetallic particles in grain boundaries that were dissolved selectively, connected, and became bigger. Electrochemically, the dissolution sequence follows the order of Mg > Al > Zn, with magnesium dissolving first at the η'-phase, primarily located at the grain boundaries, followed by aluminum dissolution of the matrix. This observation is in parallel to the EDS maps, which show a depletion of Mg and Al in the affected regions. In this localized electrochemical cell, other elements, such as Cu and Ti, act as cathodic sites. Notably, the EDS map shows the absence of Ti in corrosion products, indicating that it does not play a significant role in the corrosion process. This is consistent with the well-documented behavior of titanium, which forms a stable and protective oxide layer (TiO_2) in chloride electrolytes, effectively reducing its corrosion rate, even when in contact with more noble metals like copper [41,42].

3.3. Corrosive immersion test

In order to evaluate the susceptibility of the AM7075 alloy samples to exfoliation corrosion, an exfoliation corrosion test was conducted in a standardized EXCO (exfoliation corrosion ASTM G34) solution. This solution is widely recognized for its ability to accelerate exfoliation, simulating conditions that can lead to the degradation of the alloy's surface layer due to localized corrosion. The samples were immersed 24 h at room temperature. The test aimed to simulate the impact of aggressive, chloride-rich environments typically encountered in aerospace and marine applications, where corrosion is a major concern. Fig. 12 displays the cross-section view of the AM7075–0 alloy after corrosive exposure. This figure shows localized corrosion composed of cavities and trenches. It is important to notice that the attack propagated along the grain boundaries and the defects penetrated the alloy. The

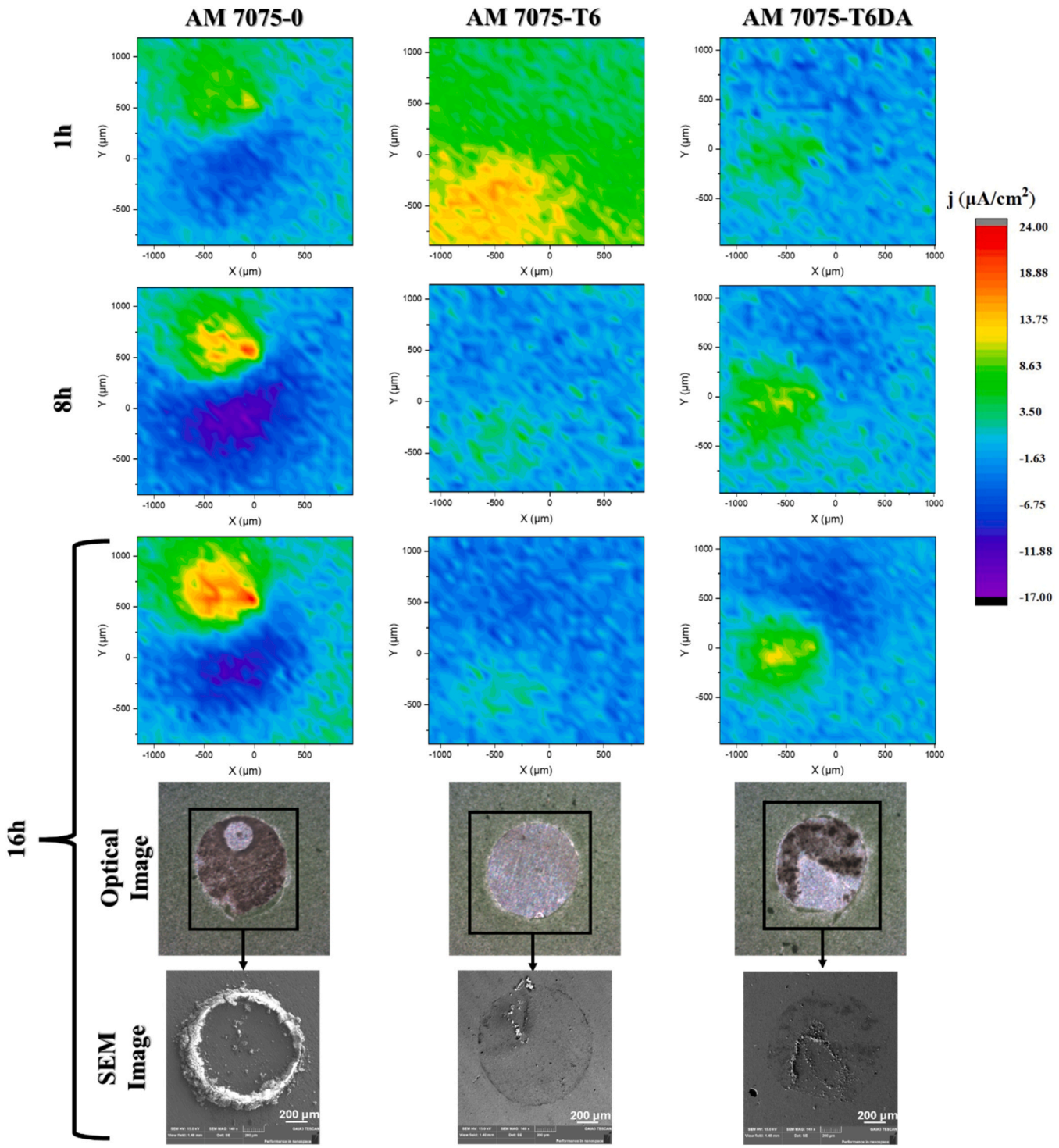

Fig. 10. SVET maps, optical images, and FESEM micrographs of the AM 7075 alloys after 16 h of immersion in 15 mM NaCl electrolyte.

AM7075–0 alloy presented a selective corrosion attack at grains, that spread by intergranular corrosion (indicated by yellow arrows), but developed transgranular corrosion (indicated by white arrows). The literature indicates the susceptibility to intergranular corrosion for AA7075 alloys [1,22,37,40,43,44]. This susceptibility is attributed to the presence of nanometric η′-phase (which nominally $MgZn_2$) precipitates, which is the major strengthening phase, and η($MgZn_2$) precipitate distribution at the grain boundaries [1,7,22,37]. The main elements (Mg and Zn) in this intermetallic contribute to decreasing the potential difference between the η phase and the α-Al matrix, a small quantity of Cu is additionally dissolved in the η-phase [37]. As observed earlier in the EDS analysis, Zn, Mg, and Cu were found in the fine network located in the grain boundaries. In the EDS maps, in Fig. 7(b), it is apparent that Cu is separated at the grain boundaries while Zn is uniformly distributed throughout the Al matrix. The remaining magnesium is employed for producing intermetallic complexes at the grain boundaries, while some of it dissolves in the Al matrix. In contact with the aggressive, chloride-rich environments, a preferential dealloying of $MgZn_2$ (anodic in relation to Cu and Al-matrix) provides a path for aggressive solution penetration and the remaining Cu undergoes a role

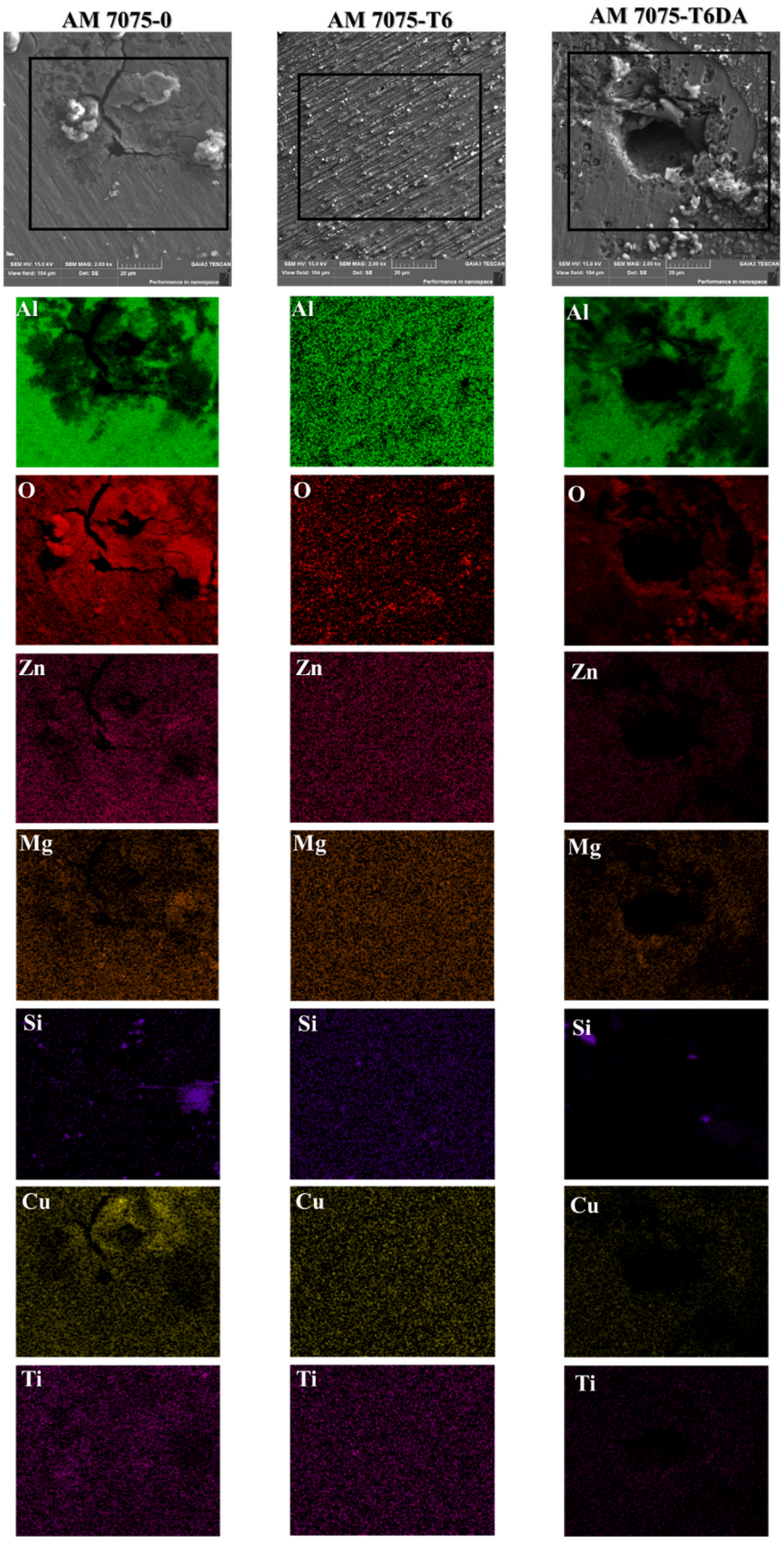

Fig. 11. SEM and Elemental EDS maps of corrosion of the samples after immersion in naturally aerated 15 mM NaCl electrolyte solution after exposure of 16 h.

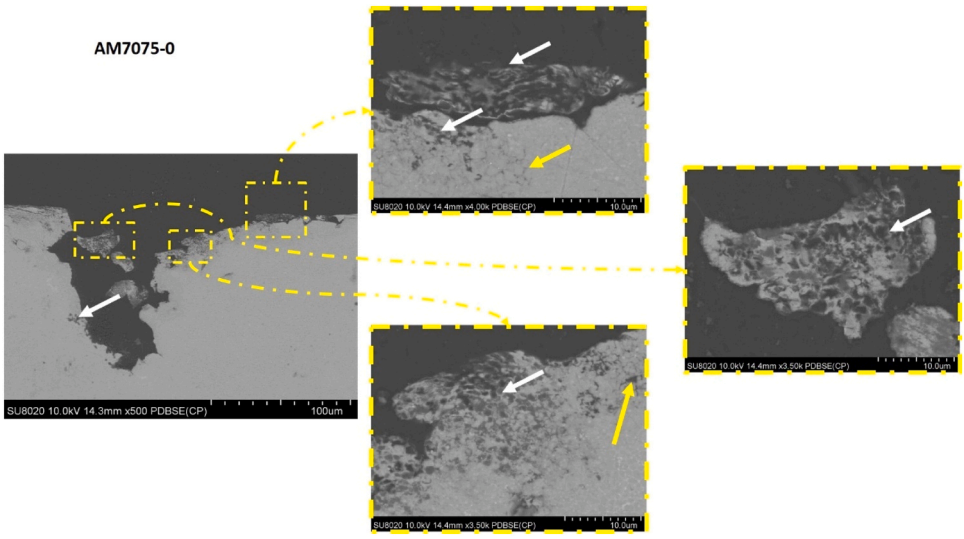

Fig. 12. SEM surface microscopy observed after AM7075–0 exposure for 24 h in Exco solution.

for pitting, and intergranular and transgranular corrosion.

Fig. 13 displays the cross-section view of the AM7075-T6 alloy after corrosive exposure. The figure shows that after the T6 treatments an intergranular corrosion attack propagated along the grain boundaries, and defects penetrated the alloy. It is worth noticing that transgranular attack was not observed after the heat treatments. As for AM7075–0, the preferential dealloying of $MgZn_2$ particles (anodic in relation to Cu and Al-matrix) located at the grain boundaries provides a path for aggressive solution penetration. However, as observed earlier in Fig. 6, AM7075-T6 does not show the fine intermetallic network, as AM7075–0 instead presents coarse intermetallic particles. The AM7075-T6DA, Fig. 14, exhibits a similar behavior. As was noted earlier in the EDS investigation, the Cu in these surfaces (AM7075-T6 and AM7075-T6DA) is concentrated in the coarse intermetallic particles, in contrast to AM7075–0. A preferential dealloying of $MgZn_2$ particles (anodic in relation to Cu and Al-matrix) in these samples creates a pathway for aggressive solution penetration in chloride-rich environments. This solution reaches Cu-rich coarse intermetallic particles, which are cathodic in relation to Al-matrix, initiating a corrosive attack in the borders of the particles consuming the anodic Al-matrix, indicated with white arrows in Figs. 13 and 14. These particles participate in pitting and localized corrosion.

Fig. 15 shows the comparison bar plot of weight-loss measurements after 24 h of exposure to Exco solution. The weight loss corresponding to the AM7075-T6 was 13.7 g/m^2, slightly lower than presented by AM7075–0 and AM7075-T6DA, at 14.9 g/m^2 and 15.1 respectively. This result shows that corrosion resistance of the T6 treated samples is improved and agrees with the EIS and SVET results, presented earlier.

3.4. Mechanical characterization

Part AM7075–0 exhibits a hardness of 115 ± 2 HV_5. The two heat treatments increase the hardness by 35 %, to reach 154 ± 5 HV_5 and 153 ± 2 HV_5 for AM7075-T6 and AM7075-T6DA parts respectively. The increase in hardness is explained by the strengthening effects of 7xxx aluminum series (precipitation hardening process) as the heat treatments modify the size and dispersion of the precipitates and reduce the residual stresses obtained after 3D printing [27,38].

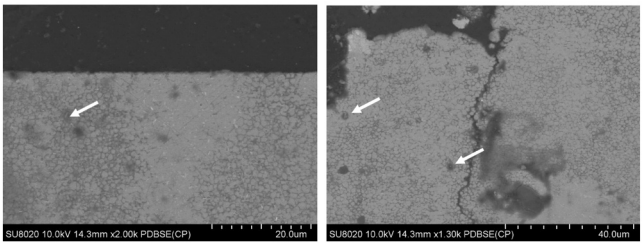

Fig. 13. SEM surface microscopy observed after AM7075-T6 exposure for 24 h in Exco solution.

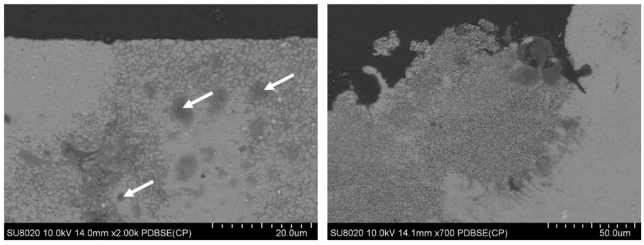

Fig. 14. SEM surface microscopy observed after AM7075-T6DA exposure for 24 h in Exco solution.

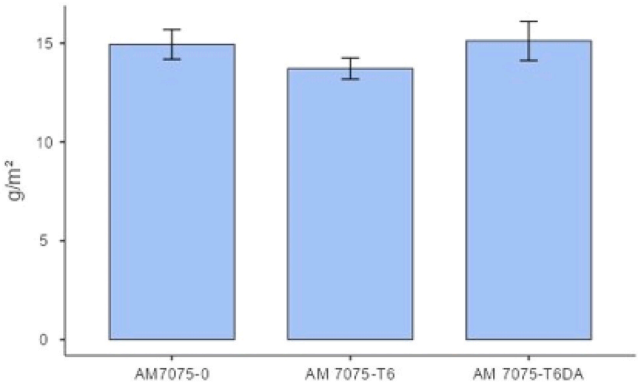

Fig. 15. Weight-loss bar plot samples after exposure for 24 h in Exco solution.

4. Discussion

The results presented in this work highlight the impact of heat treatments on the corrosion resistance AM7075-Ti alloys. The study identified that surface modification after heat treatments has a special role in the corrosion modes and resistance. As observed in the SEM

images (Fig. 6), AM7075–0 has a fine intermetallic network surrounding the grain boundaries. As indicated in the EDS analysis, (Figs. 7, 8, and 9) and EBSD phase maps, (Fig. 5), the network is mainly composed of Cu (4.7 %), Mg (3.4 %), and Zn (9.5 %), and the literature indicates that this fine network is mainly composed by nanometric η′-phase (which nominally $MgZn_2$) precipitates, η($MgZn_2$) and a small quantity of Cu is additionally dissolved in the phases [37]. As previously discussed, Mg-rich particles are anodic relative to the Al matrix and Cu-rich particles, which enables them to sustain anodic currents leading to high Mg dissolution rates [1,25,45]. In contrast, Cu-rich particles are cathodic relative to both the Al-matrix and Mg-rich particles, and thus can promote dissolution of the Al matrix and Mg particles, which means that these particles are capable of sustaining cathodic currents with result in Al-matrix and $MgZn_2$ particle dissolution. When exposed to a corrosive

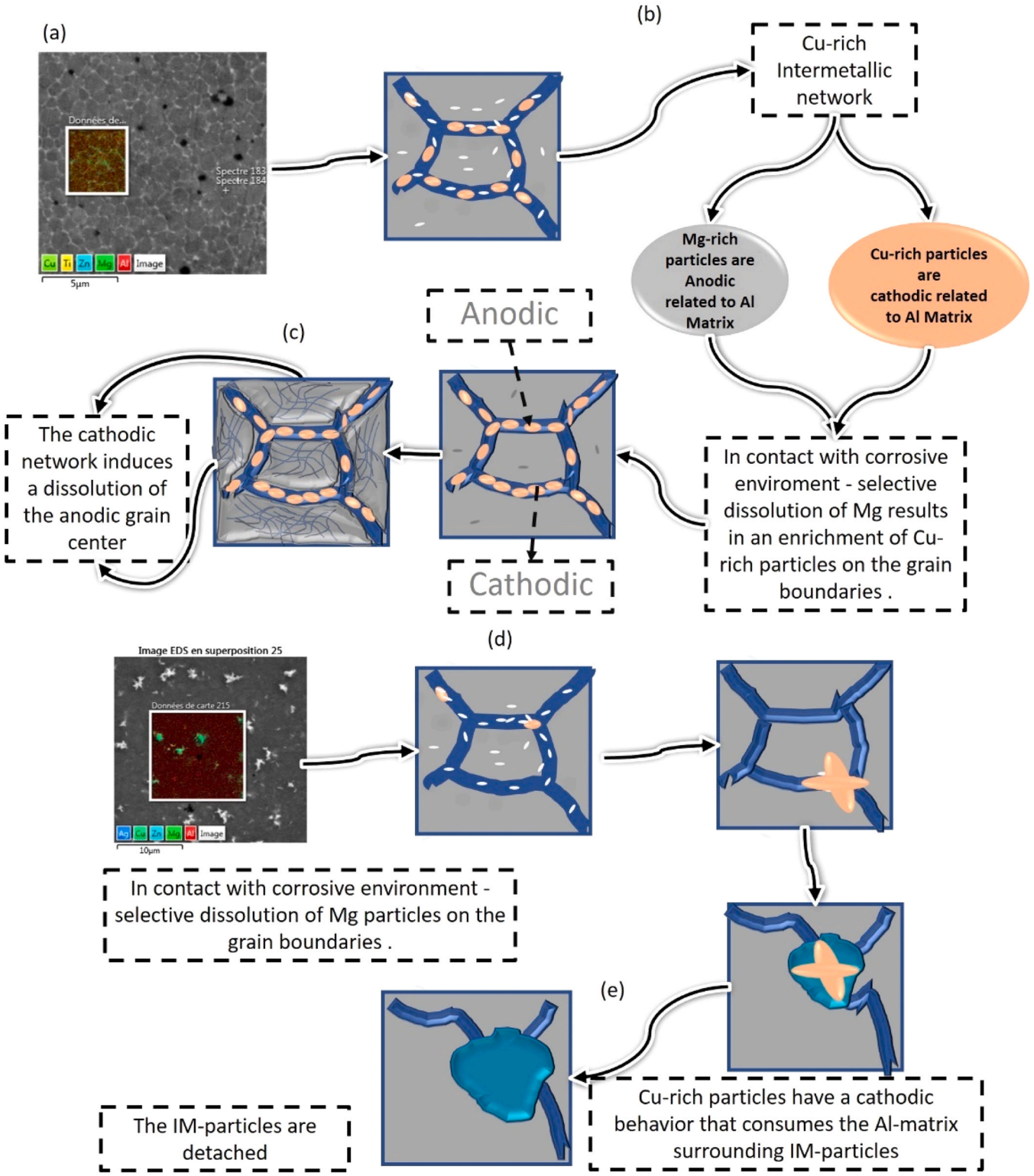

Fig. 16. Proposed corrosion mechanism.

environment, selective corrosion of anodic $MgZn_2$ particles (nanometric and coarse intermetallic particles) starts with an electrochemical cell between Cu particles and Al-matrix. In a second step, after the consumption of these particles, a remnant of Cu-particles is located at the borders, creating a cathodic network related to the Al matrix at the grain center. An electrochemical cell between the borders and the centers results in a dissolution of the Al matrix of the grain center as transgranular corrosion (Fig. 12). Following heat treatments, the previously fine intermetallic network transforms into coarser intermetallic particles, as observed in SEM images (Fig. 6). In the heat-treated sample, corrosion is propagated by the grain boundaries, as an effect of nanometric η'-phase precipitates and develops surrounding the coarse intermetallic particles. Upon exposure to a corrosive environment, $MgZn_2$ selective dealloying occurs. After the consumption, these Cu-rich particles (cathodic related to Al-matrix) start a local dissolution surrounding the particles, as observed in Figs. 13 and 14 (indicated by white arrows).

Based on the experimental results, a corrosion mechanism (Fig. 16), is proposed to explain the behavior of AM7075 alloys before and after heat treatments. In the as-built condition (AM7075–0 - Fig. 16(a)), the microstructure features a fine intermetallic network composed mainly of Cu, Mg, and Zn, distributed along the grain boundaries. These intermetallics, particularly the nanometric η' phase ($MgZn_2$), are electrochemically active in a corrosive environment (Fig. 16(b)). The Mg-rich particles, being anodic relative to both the Al matrix and Cu-rich particles, dissolve preferentially, initiating localized corrosion. This selective dissolution of Mg establishes micro-galvanic cells between the anodic Mg-rich regions and the cathodic Cu-rich areas. As the corrosion process progresses and the Mg is consumed, the remaining Cu particles, now concentrated at the grain boundaries, form a cathodic network (Fig. 16(c)). This arrangement promotes further galvanic activity, now driving the anodic dissolution of the Al matrix at the center of the grains. The result is a characteristic transgranular corrosion attack, where the central region of the grains is selectively corroded, as observed in the microstructural analysis. After heat treatment, the fine intermetallic network is transformed into coarse intermetallic particles dispersed throughout the matrix, (Fig. 16(d)). Around these particles, nanometric η' precipitates tend to form. Upon exposure to a corrosive medium, selective dealloying of $MgZn_2$ IM particles again occurs. Once these particles are depleted, the Cu-rich particles—being cathodic relative to the surrounding Al matrix—facilitate localized dissolution of the matrix in their vicinity. This leads to the development of pitting and intergranular corrosion paths.

The weight-loss after immersion tests and electrochemical results indicate a superior corrosion resistance for the AM7075-T6 compared to AM7075-T6DA. This improved corrosion resistance could be attributed to the fact that the double aging heat process applied to AM7075 increased the amount of Cu (4.4 % for T6 and 30 % for T6DA) and Mg (2.1 % for T6 and 8.1 % for T6DA) in the coarse intermetallic particles. The presence of this high amount of Cu particles on the surface decreases the resistance of the alumina passive layer, as observed using EIS measurements and SVET analysis.

5. Conclusion

This study has highlighted the critical role of heat treatments in influencing the corrosion resistance and mechanical properties of AM7075-Ti alloys. The results show that the surface modifications induced by the heat treatments considerably alter the corrosion mechanisms by affecting the intermetallic network at the grain boundaries. The proposed corrosion mechanism reveals that Mg- and Cu-rich particles within the network contribute to selective corrosion through electrochemical interactions, leading to transgranular corrosion of the Al-matrix. The transformation of the fine intermetallic network into coarser particles after heat treatment further promotes corrosion along grain boundaries.

The findings also indicate that heat-treated AM7075-Ti alloys, particularly AM7075-T6, exhibit improved corrosion resistance and enhanced hardness, owing to the redistribution of Cu and Mg within the intermetallic phases.

CRediT authorship contribution statement

Sajjad Akbarzadeh: Writing – original draft, Methodology, Formal analysis. **Rafael Emil Klumpp:** Writing – review & editing, Writing – original draft, Visualization, Validation, Supervision, Resources, Project administration, Methodology, Investigation, Formal analysis, Data curation, Conceptualization. **Delaunois Fabbiene:** Writing – review & editing, Methodology. **Alexandre Megret:** Methodology, Formal analysis. **Vedi Ölmez:** Methodology, Formal analysis. **Thomas Kairet:** Methodology, Formal analysis. **Marie-Georges Olivier:** Writing – review & editing, Writing – original draft, Visualization, Validation, Supervision, Resources, Project administration, Methodology, Investigation, Funding acquisition, Formal analysis, Data curation, Conceptualization.

Declaration of Competing Interest

The authors declare that they have no known competing financial interests or personal relationships that could have appeared to influence the work reported in this paper.

Acknowledgements

The authors are thankful to program Win2Wal (2023) of the Service Public de Wallonie for financial support for this project (*OptiSurFam*) and the Materia Nova – Material R&D for the scanning electron microscopy characterization.

Appendix A. Supporting information

Supplementary data associated with this article can be found in the online version at doi:10.1016/j.jallcom.2025.183276.

References

[1] G. Sander, J. Tan, P. Balan, O. Gharbi, D.R. Feenstra, L. Singer, S. Thomas, R. G. Kelly, J.R. Scully, N. Birbilis, Corrosion of additively manufactured alloys: a review, Corrosion 74 (2018) 1318–1350, https://doi.org/10.5006/2926.

[2] N.T. Aboulkhair, M. Simonelli, L. Parry, I. Ashcroft, C. Tuck, R. Hague, Progress in materials science 3D printing of aluminium alloys: additive manufacturing of aluminium alloys using selective laser melting, Prog. Mater. Sci. 106 (2019) 100578, https://doi.org/10.1016/j.pmatsci.2019.100578.

[3] A. Bandyopadhyay, Y. Zhang, S. Bose, Recent developments in metal additive manufacturing, Curr. Opin. Chem. Eng. 28 (2020) 96–104, https://doi.org/10.1016/j.coche.2020.03.001.

[4] R.I. Revilla, J. Liang, I. De Graeve, Local corrosion behavior of additive manufactured AlSiMg alloy assessed by SEM and SKPFM, J. Electrochem. Soc. 164 (2017) C27–C35, https://doi.org/10.1149/2.0461702jes.

[5] M. Cabrini, S. Lorenzi, T. Pastore, S. Pellegrini, M. Pavese, P. Fino, E.P. Ambrosio, F. Calignano, D. Manfredi, Corrosion resistance of direct metal laser sintering AlSiMg alloy, Surf. Interface Anal. (2016), https://doi.org/10.1002/sia.5981.

[6] M. Cabrini, S. Lorenzi, T. Pastore, S. Pellegrini, D. Manfredi, P. Fino, S. Biamino, C. Badini, Journal of materials processing technology evaluation of corrosion resistance of al – 10Si – mg alloy obtained by means of direct metal laser sintering, J. Mater. Process. Tech. 231 (2016) 326–335, https://doi.org/10.1016/j.jmatprotec.2015.12.033.

[7] J. ying Hu, P. Liu, S. yu Sun, Y. hua Zhao, Y. bin Zhang, Y. shuang Huo, Relation between heat treatment processes and microstructural characteristics of 7075 al alloy fabricated by SLM, Vacuum 177 (2020), https://doi.org/10.1016/j.vacuum.2020.109404.

[8] C. Örnek, Additive manufacturing–a general corrosion perspective, Corros. Eng. Sci. Technol. 53 (2018) 531–535, https://doi.org/10.1080/1478422X.2018.1511327.

[9] F. Simchen, M. Sieber, T. Lampke, Electrolyte influence on ignition of plasma electrolytic oxidation processes on light metals, Surf. Coat. Technol. 315 (2017) 205–213, https://doi.org/10.1016/j.surfcoat.2017.02.041.

[10] J.H. Martin, B.D. Yahata, J.M. Hundley, J.A. Mayer, T.A. Schaedler, T.M. Pollock, 3D printing of high-strength aluminium alloys, Nature 549 (2017) 365–369, https://doi.org/10.1038/nature23894.

[11] M. Karg, B. Ahuja, S. Kuryntsev, A. Gorunov, M. Schmidt, Processability of high strength aluminium-copper alloys AW-2022 and 2024 by laser beam melting in powder bed, 25th annu, Int. Solid Free. Fabr. Symp. Addit. Manuf. Conf. SFF 2014 (2014) 420–436.
[12] S.Z. Uddin, L.E. Murr, C.A. Terrazas, P. Morton, D.A. Roberson, R.B. Wicker, Processing and characterization of crack-free aluminum 6061 using high-temperature heating in laser powder bed fusion additive manufacturing, Addit. Manuf. 22 (2018) 405–415, https://doi.org/10.1016/j.addma.2018.05.047.
[13] B. Ahuja, M. Karg, K.Y. Nagulin, M. Schmidt, Fabrication and characterization of high strength Al-Cu alloys processed using laser beam melting in metal powder bed, Phys. Procedia 56 (2014) 135–146, https://doi.org/10.1016/j.phpro.2014.08.156.
[14] S. Youmin, R. Xiaohua, C. Zhaojie, The degradation mechanism of phenol induced by ozone in wastes system, (2012) 3821–3830. https://doi.org/10.1007/s00894-012-1376-5.
[15] F. Jiang, L. Tang, H. Ye, Z. Yang, The role of TiH2 on microstructure and mechanical properties of Al–Zn–Mg–Cu alloy fabricated by laser powder bed fusion, Mater. Sci. Eng. A 869 (2023), https://doi.org/10.1016/j.msea.2023.144819.
[16] A.A. Akinwande, D. Moskovskikh, V. Romanovski, Enhancing mechanical and damping performance of 3D-printed aluminium-7075 with shape memory high-entropy alloy (SMHEA): parametric optimization and mathematical modeling, Int. J. Adv. Manuf. Technol. 130 (2024) 369–383, https://doi.org/10.1007/s00170-023-12651-z.
[17] T. Kairet, O. Rigo, A. Hemberg, T. Godefroid, Metal-coated aluminium alloy particles, process for producing same, and additive process using the coated, WO2025002659, Alum. Alloy Particles (2025), ⟨https://patentscope.wipo.int/search/en/WO2025002659⟩. WO2025002659.
[18] Q. Tan, Z. Fan, X. Tang, Y. Yin, G. Li, D. Huang, J. Zhang, Y. Liu, F. Wang, T. Wu, X. Yang, H. Huang, Q. Zhu, M.X. Zhang, A novel strategy to additively manufacture 7075 aluminium alloy with selective laser melting, Mater. Sci. Eng. A 821 (2021) 141638, https://doi.org/10.1016/j.msea.2021.141638.
[19] R.E. Klumpp, S. Akbarzadeh, J.V. de Sousa Araujo, M.F. Gonon, F. Delaunois, I. Costa, M.G. Olivier, Correlating corrosion modes with the microstructure of the 2XXX series alloys: a comparative approach, Surf. Interface Anal. 56 (2024) 643–653, https://doi.org/10.1002/sia.7321.
[20] A. Azarniya, A.K. Taheri, K.K. Taheri, Recent advances in ageing of 7xxx series aluminum alloys: a physical metallurgy perspective, J. Alloy. Compd. 781 (2019) 945–983, https://doi.org/10.1016/j.jallcom.2018.11.286.
[21] S.K. Kairy, O. Gharbi, J. Nicklaus, D. Jiang, C.R. Hutchinson, N. Birbilis, On the characterization of a hitherto unreported icosahedral quasicrystal phase in additively manufactured aluminum alloy AA7075, Metall. Mater. Trans. A Phys. Metall. Mater. Sci. 50 (2019) 529–533, https://doi.org/10.1007/s11661-018-5025-1.
[22] O. Gharbi, S.K. Kairy, Microstructure and corrosion evolution of additively manufactured aluminium alloy AA7075 as a function of ageing, Npj Mater. Degrad. (2019), https://doi.org/10.1038/s41529-019-0101-6.
[23] O. Gharbi, D. Jiang, D.R. Feenstra, S.K. Kairy, Y. Wu, C.R. Hutchinson, N. Birbilis, On the corrosion of additively manufactured aluminium alloy AA2024 prepared by selective laser melting, Corros. Sci. 143 (2018) 93–106, https://doi.org/10.1016/j.corsci.2018.08.019.
[24] J. lei Huang, J. feng Li, D. yang Liu, R. feng Zhang, Y. lai Chen, X. hu Zhang, P. cheng Ma, R.K. Gupta, N. Birbilis, Correlation of intergranular corrosion behaviour with microstructure in Al-Cu-Li alloy, Corros. Sci. 139 (2018) 215–226, https://doi.org/10.1016/j.corsci.2018.05.011.
[25] N. Birbilis, R.G. Buchheit, Electrochemical characteristics of intermetallic phases in aluminum alloys an experimental survey and discussion, B140–B151, J. Electrochem. Soc. 152 (2005), https://doi.org/10.1149/1.1869984.
[26] Y. Liu, A. Laurino, T. Hashimoto, X. Zhou, P. Skeldon, G.E. Thompson, G. M. Scamans, C. Blanc, W.M. Rainforth, M.F. Frolish, Corrosion behaviour of mechanically polished AA7075-T6 aluminium alloy, Surf. Interface Anal. 42 (2010) 185–188, https://doi.org/10.1002/sia.3136.
[27] Y. Su, Y. Wang, J. Shi, Microstructure and mechanical properties of laser DED produced crack-free al 7075 alloy: effect of process parameters and heat treatment, Mater. Sci. Eng. A 857 (2022), https://doi.org/10.1016/j.msea.2022.144075.
[28] J. liang Zhang, J. liang Ye, B. Song, R. di Li, Y. sheng Shi, Comparative study on microstructure and electrochemical corrosion resistance of Al7075 alloy prepared by laser additive manufacturing and forging technology, J. Cent. South Univ. 28 (2021) 1058–1067, https://doi.org/10.1007/s11771-021-4679-9.
[29] V.K. Beura, A. Sharma, Y. Karanth, S. Sharma, K. Solanki, Corrosion behavior of 7050 and 7075 aluminum alloys processed by reactive additive manufacturing, Electrochim. Acta 470 (2023), https://doi.org/10.1016/j.electacta.2023.143357.
[30] J. Liu, Y. Miao, R. Wu, C. Wei, Y. Zhao, Y. Wu, Q. Deng, Effect of heat treatment on microstructure, mechanical properties and corrosion resistance of 7075 aluminum alloys fabricated by improved friction stir additive manufacturing, J. Alloy. Compd. 1007 (2024), https://doi.org/10.1016/j.jallcom.2024.176512.
[31] G. Choi, H. Chae, Y.S. Kim, S.K. Hong, E. Shin, S.Y. Lee, Additive manufacturing of Si-Added 7075 aluminum alloys: microstructural, mechanical, and electrochemical properties via heat treatment, Materials 18 (2025), https://doi.org/10.3390/ma18071544.
[32] K.G. Prashanth, B. Debalina, Z. Wang, P.F. Gostin, A. Gebert, M. Calin, M. Kamaraj, S. Scudino, J. Eckert, Tribological and corrosion properties of al – 12Si produced by selective laser melting, J. Mater. Res. 29 (2014) 2044–2054, https://doi.org/10.1557/jmr.2014.133.
[33] S.B. Pankade, D.S. Khedekar, C.L. Gogte, The influence of heat treatments on electrical conductivity and corrosion performance of AA 7075-T6 aluminium alloy, Procedia Manuf. 20 (2018) 53–58, https://doi.org/10.1016/j.promfg.2018.02.007.
[34] R. Revilla, I. de Graeve, Influence of si content on the microstructure and corrosion behavior of additive manufactured Al-Si alloys, J. Electrochem. Soc. 165 (13) (2018) C926–C932, https://doi.org/10.1149/2.0101814jes.
[35] P. Fathi, M. Mohammadi, X. Duan, A.M. Nasiri, A comparative study on corrosion and microstructure of direct metal laser sintered AlSi10Mg _ 200C and die cast A360. 1 aluminum, J. Mater. Process. Tech. 259 (2018) 1–14, https://doi.org/10.1016/j.jmatprotec.2018.04.013.
[36] J.C. Pereira, E. Gil, L. Solaberrieta, M. San Sebastián, Y. Bilbao, P.P. Rodríguez, Comparison of AlSi7Mg0.6 alloy obtained by selective laser melting and investment casting processes: microstructure and mechanical properties in as-built/as-cast and heat-treated conditions, Mater. Sci. Eng. A 778 (2020), https://doi.org/10.1016/j.msea.2020.139124.
[37] Y. Zhang, H. Yang, P. Sun, R. Huang, S. Zheng, Y. Duan, M. Li, Effect of aging time on precipitation of MgZn2 and microstructure and properties of 7075 aluminum alloy, J. Mater. Eng. Perform. 33 (2024) 6601–6611, https://doi.org/10.1007/s11665-023-08426-y.
[38] S.V. Emani, J. Benedyk, P. Nash, D. Chen, Double aging and thermomechanical heat treatment of AA7075 aluminum alloy extrusions, J. Mater. Sci. 44 (2009) 6384–6391, https://doi.org/10.1007/s10853-009-3879-8.
[39] C. Wang, T. Zhang, H. Yin, Z. Lü, Effect of aging treatment on microstructure and properties of 7075 aluminum alloy, Jinshu Rechuli/Heat. Treat. Met. 42 (2017) 87–90, https://doi.org/10.13251/j.issn.0254-6051.2017.09.019.
[40] J. feng Li, Z. wei Peng, C. xing Li, Z. qiang Jia, W. jing Chen, Z. qiao Zheng, Mechanical properties, corrosion behaviors and microstructures of 7075 aluminium alloy with various aging treatments, Trans. Nonferrous Met. Soc. China (Engl. Ed. 18 (2008) 755–762, https://doi.org/10.1016/S1003-6326(08)60130-2.
[41] N. Birbilis, R.G. Buchheit, Electrochemical characteristics of intermetallic phases in aluminum alloys, J. Electrochem. Soc. 152 (2005) B140, https://doi.org/10.1149/1.1869984.
[42] K. Dong, Y. Song, F. Chang, E.H. Han, Galvanic corrosion mechanism of Ti-Al coupling: the impact of passive films on the coupling effect, Electrochim. Acta 462 (2023), https://doi.org/10.1016/j.electacta.2023.142662.
[43] J.B. Lumsden, M.W. Mahoney, G. Pollock, C.G. Rhodes, Intergranular corrosion following friction stir welding of aluminum alloy 7075-T651, Corrosion 55 (1999) 1127–1135.
[44] Y. long Ma, X. rong Zhou, X. min Meng, W. jiu Huang, Y. Liao, X. li Chen, Y. nan Yi, X. xin Zhang, G.E. Thompson, Influence of thermomechanical treatments on localized corrosion susceptibility and propagation mechanism of AA2099 Al–Li alloy, Trans. Nonferrous Met. Soc. China (Engl. Ed. 26 (2016) 1472–1481, https://doi.org/10.1016/S1003-6326(16)64252-8.
[45] J.A. Lyndon, R.K. Gupta, M.A. Gibson, N. Birbilis, Electrochemical behaviour of the b -phase intermetallic (Mg 2 Al 3) as a function of ph as relevant to corrosion of aluminium – magnesium alloys, Corros. Sci. 70 (2013) 290–293, https://doi.org/10.1016/j.corsci.2012.12.022.